Wind-driven evolution of the North Pacific subpolar gyre over the last deglaciation

William R Gray[1,2]*, Robert CJ Wills[3], James WB Rae[2], Andrea Burke[2], Ruza F Ivanovic[4], William HG Roberts[5], David Ferreira[6], Paul J Valdes[7]

[1]Laboratoire des Sciences du Climat et de l'Environnement (LSCE/IPSL), Gif-sur-Yvette, France

[2]School of Earth and Environmental Science, University of St Andrews, UK

[3]Department of Atmospheric Sciences, University of Washington, USA

[4]School of Earth & Environment, University of Leeds, UK

[5]Geography and Environmental Sciences, Northumbria University, UK

[6]Department of Meteorology, University of Reading, UK

[7]School of Geographical Sciences, University of Bristol, UK

*corresponding author: william.gray@lsce.ipsl.fr

Key points

- Planktic foraminiferal $\delta^{18}O$ data indicate that the North Pacific subpolar gyre expanded southward by ~3° during the Last Glacial Maximum
- Climate models show that changes in gyre extent/strength are driven by the response of the westerlies to ice sheet albedo and topography
- Proxy data and model simulations indicate that the gyre boundary and winds began to migrate northward at ~17-16 ka, during Heinrich Stadial 1

Abstract

North Pacific atmospheric and oceanic circulations are key missing pieces in our understanding of the reorganisation of the global climate system since the Last Glacial Maximum (LGM). Here, using a basin-wide compilation of planktic foraminiferal $\delta^{18}O$, we show that the North Pacific subpolar gyre extended ~3° further south during the LGM, consistent with sea surface temperature and productivity proxy data. Analysis of an ensemble of climate models indicates that the expansion of the subpolar gyre was associated with a substantial gyre strengthening. These gyre circulation changes were driven by a southward shift in the mid-latitude westerlies and increased wind-stress from the polar easterlies. Using single-forcing model runs, we show these atmospheric circulation changes are a non-linear response to the combined topographic and albedo effects of the Laurentide Ice Sheet. Our reconstruction suggests the gyre boundary (and thus westerly winds) began to migrate northward at ~17-16 ka, during Heinrich Stadial 1.

Plain language summary

Despite the North Pacific's importance in the global climate system, changes in the circulation of this region since the last ice age are poorly understood. Today, the North Pacific Ocean has very different properties north and south of ~40°N: to the south, the warm surface waters form a circulation cell that moves clockwise (the subtropical gyre); to the north, the cold surface waters form a circulation cell that moves anti-clockwise (the subpolar gyre). This difference in surface ocean circulation north and south of ~40°N is determined by the wind patterns. Here, using a compilation of oxygen isotopes measured in the carbonate shells of fossil plankton from sediment cores across the basin, which tracks changes in the spatial pattern of temperature, we reconstruct how the position of the boundary between the gyres

changed since the last ice age. Our results show that the boundary between the gyres was shifted southward by ~3° during the last ice age; this indicates that the westerly winds were also shifted southward at this time. Using numerical simulations of the climate, we find that this ice age shift in the westerly winds is primarily due to the presence of a large ice sheet over North America.

1. Introduction

Despite the North Pacific's importance in the global climate system, the reorganisation of surface ocean and atmosphere in this region during the Last Glacial Maximum (LGM, ~20 ka) and the last deglaciation (~10-20 ka, 'the deglaciation' from here on) remain poorly constrained. Changes in atmospheric and surface ocean circulation within the North Pacific are potentially important drivers of observed changes in the overturning circulation and biogeochemistry of the North Pacific during the LGM and deglaciation, suggested to play a role in regulating atmospheric CO_2 (Keigwin, 1998; Okazaki *et al*., 2010; Rae *et al.*, 2014; Gray *et al*., 2018). The overturning and gyre circulations are also important influences on poleward ocean heat transport. Large changes in the hydroclimate of western North America during the LGM and the deglaciation (e.g. Oviatt et al., 1999; Nelson *et al*., 2005; Lyle *et al.*, 2012; McGee *et al*., 2012; Kirby *et al*., 2013; Ibarra *et al*., 2014) have been suggested to result from the reorganisation of North Pacific atmospheric circulation (e.g. Oster *et al*., 2015; Wong *et al*., 2016; Lora *et al.*, 2017; Lora, 2018), with early modelling work suggesting a southward displacement of the westerly jet with the presence of the Laurentide Ice Sheet (Manabe & Brocolli, 1985; Bartlein et al., 1998). However, evidence for this atmospheric reorganisation has not yet been identified in marine records.

Driven by the opposite signs of the climatological wind stress curl ($\nabla \times \tau$), the subtropical and subpolar gyres of the North Pacific Ocean have vastly different physical and chemical properties (Boyer *et al*., 2013; Key *et al*., 2015). The boundary between the gyres (defined as the point between the gyres at which the barotropic streamfunction [$\Psi_{barotropic}$] = 0) is determined by Sverdrup balance and occurs where $\nabla \times \tau$ integrated from the eastern boundary of the basin is zero (Sverdrup, 1947; Deser *et al*., 1999). Today, the gyre boundary (which broadly determines the position of the subarctic front) is nearly zonal and lies at ~40 °N, approximately following the local $\nabla \times \tau = 0$ line. South of ~40°N, anticyclonic wind stress curl in the subtropical gyre (STG) results in Ekman pumping (downwelling), allowing warm, nutrient-poor, surface waters to accumulate. North of ~40°N, cyclonic wind stress curl in the subpolar gyre (SPG) results in Ekman suction (upwelling), bringing cold, nutrient-rich, waters from the oceans interior into the surface. Surface ocean chlorophyll concentrations are order of magnitude higher in the SPG compared to the STG. The gyre circulation also dominates ocean heat transport in the Pacific (Forget and Ferreira, 2019). The relative extent and the strength of the gyres therefore exerts a large influence over basin-wide ecology, biogeochemistry, and climate.

Coupled climate models predict a ~60% increase in wind stress curl within the subpolar North Pacific under glacial forcings compared to pre-industrial forcings (Gray *et al*., 2018). By Sverdrup balance (Sverdrup, 1947), this should result in a large and predictable response in gyre circulation. Despite some early work suggesting the subarctic front may have shifted southward during glacial times (Thompson and Shackleton, 1980; Sawada and Handa, 1998), little is known about gyre circulation over the deglaciation. Here, we use meridional profiles of planktic foraminiferal $\delta^{18}O$ to reconstruct the position of the gyre boundary over the deglaciation. Given the relatively simple dynamical link between gyre circulation and wind stress, our gyre boundary reconstruction also helps constrain the deglacial reorganisation of the atmospheric circulation. We use an ensemble of climate models forced by a range of boundary conditions to further explore the causes and implications of our gyre boundary reconstruction for the atmospheric and near-surface ocean circulations within the North Pacific.

2. Methods

2.1 $\delta^{18}O$ as a tracer of gyre circulation

The large (~20 °C) sea surface temperature (SST) difference between the gyres (Boyer *et al.*, 2013) allows us to use meridional profiles of $\delta^{18}O$ in planktic foraminiferal calcite ($\delta^{18}O_{calcite}$) to trace the gyre boundary (supporting information). This temperature difference between the gyres drives a calcite-water fractionation ($\delta^{18}O_{calcite-water}$) that is ~6 ‰ greater in the SPG than the STG (Figure 1d). Therefore, although the $\delta^{18}O$ of seawater ($\delta^{18}O_{water}$) is ~1 ‰ lighter in the SPG compared to the STG due to its lower salinity (~1.5 PSU; Figure 1c), $\delta^{18}O_{calcite}$ is ~5 ‰ higher in the SPG than the STG (Figure 1e). The two gyres are thus clearly delineated in the $\delta^{18}O$ of planktic foraminiferal calcite predicted using modern temperature and $\delta^{18}O_{water}$ (Figure 1e), with the steepest meridional gradient in $\delta^{18}O_{calcite}$ at the gyre boundary (Figure 1f). While there are likely to be local changes in $\delta^{18}O_{water}$ across the basin over the deglaciation, a salinity difference of ~15 PSU would be required to equal the temperature signal between the gyres. As no mechanism exists to drive such a salinity/$\delta^{18}O_{water}$ difference, temperature will always dominate the meridional

$\delta^{18}O_{calcite}$ gradient (Figure 1f). We can therefore use meridional profiles of $\delta^{18}O_{calcite}$ to track the position of the gyre boundary.

We compiled previously published planktic foraminiferal $\delta^{18}O_{calcite}$ records spanning the last deglaciation from the North Pacific Ocean (Figure 1; supporting information). The gyre boundary is clearly defined by the steepest meridional gradient ($\Delta\delta^{18}O_{calcite}/\Delta$Latitude) in the Holocene planktic foraminiferal $\delta^{18}O_{calcite}$ data (Figure 2; supporting information). The difference in meridional temperature gradient between the east and west of the basin is also evident in the Holocene $\delta^{18}O_{calcite}$ data (Figure 2b).

To reconstruct position the of gyre boundary over the deglaciation, we first model the $\delta^{18}O_{calcite}$ data as a function of latitude, using a general additive model (GAM) in the *mgcv* package in R (Wood, 2011; Wood *et al*., 2016) at 500 yr timesteps from 18.5 to 10.5 ka (supporting information; Figures S2-4). The smoothing term was calculated using generalised cross validation (GCV), and corroborated using Reduced Maximum Likelihood (REML), with both methods resulting in near-identical smoothing terms and model fits. We then calculate the change in gyre boundary position over the deglaciation as the latitudinal shift (x°) that minimises the Euclidian distance (L^2) between the Holocene (taken as 10.5±0.5 ka) $\delta^{18}O_{calcite}$(Lat) GAM fit and the GAM fit at each time step, computed within a 5° latitudinal band around the maximum meridional $\delta^{18}O_{calcite}$ gradient in the Holocene data (supporting information; Figure S5). The width of this latitudinal band has a negligible effect on our results (Figure S6).

We account for the effect of whole ocean changes in sea level ($\delta^{18}O_{water}$) and SST on $\delta^{18}O_{calcite}$ by subtracting the 1‰ whole ocean change in $\delta^{18}O_{water}$ (Schrag *et al.*, 2002) and the ~2°C global-mean change in SST from the PMIP3 climate model ensemble (see below), scaling the subtracted anomalies through time in proportion to the sea level curve of Lambeck et al. (2014). This scaling is most robust for $\delta^{18}O_{water}$ due to its direct correlation with global terrestrial ice volume, however the correction for global SST has very little effect and is not therefore a significant source of error. We opt to make this global-mean SST correction in order to minimise differences in $\delta^{18}O_{calcite}$ at different time steps relating to whole-ocean SST changes (i.e. from radiative forcing), rather than local SST anomalies. The calculated changes in gyre boundary position (ΔLat) are given in table S2; the reported uncertainty in ΔLat is derived by quadratically propagating the uncertainty in the $\delta^{18}O_{calcite}$(Lat) GAM fits, and is typically ±0.9° (1σ).

2.2 General circulation models

We analysed an ensemble of general circulation models forced with pre-industrial and glacial boundary conditions from the Coupled Model Intercomparison Project phase 5 (CMIP5, Taylor *et al.* 2012) and the Paleoclimate Model Intercomparison Project phase 3 (PMIP3, Braconnot *et al.* 2012). We include all four models for which both wind stress and barotropic stream function are available (supporting information). We also analyse results from a single model (HadCM3) where LGM greenhouse gases, ice sheet topography (‘green mountains’), and ice sheet albedo (‘white plains’) forcing were changed individually (Roberts and Valdes, 2017), as well as a series of HadCM3 runs where all forcings and boundary conditions are changed progressively over the deglaciation in 500 yr ‘snapshots’ (as used by

Morris *et al*., 2018), broadly following the PMIP4 protocol (Figure S8; see Ivanovic *et al*., 2016 and supporting information).

3. Results and Discussion

3.1 LGM planktic foraminiferal $\delta^{18}O$, SST, and productivity

While sites that today are located well within either the modern SPG or STG display an LGM difference in $\delta^{18}O_{calcite}$ of ~1-1.5 ‰, sites located within the transition zone between the gyres display a much greater change of up to ~3 ‰ (Figure 1). This anomalously large glacial increase in $\delta^{18}O_{calcite}$ is observed in transition zone sites in the east and west of the basin. The Holocene $\delta^{18}O_{calcite}$ of sites located in today's transition zone typically falls about half-way between the $\delta^{18}O_{calcite}$ of the SPG and STG. In contrast, during the LGM the $\delta^{18}O_{calcite}$ of these same sites is almost identical to the $\delta^{18}O_{calcite}$ of sites located well within the SPG. This pattern is indicative of a southward shift in the boundary between the SPG and STG, such that sites that are located within the transition zone today were located in (or felt a much greater influence of) the SPG during the LGM.

Analysing all data from across the basin together indicates the gyre boundary was positioned 3.1±0.9° (1σ) further south during the LGM compared with its position in the Holocene (Figure 2a). Analysing the data from east and west of 180° separately results in a smaller change in the west of 2.0±0.9°, and a greater change in the east of 6.0±1.1° (Figure 2b). To assess if the larger change in the east of the basin may be an artefact of changes in coastal upwelling, a process which could also influence the local SST (and thus $\delta^{18}O_{calcite}$) anomaly, we compare the PMIP3 ensemble mean SST near the eastern boundary of the basin to the zonal mean, and zonal mean east of 180° (Figure S9). This analysis demonstrates no anomalous cooling at the eastern margin of the basin relative to the zonal average and zonal average east of 180° in the models, suggesting that coastal upwelling is unlikely to have a significant effect on our reconstruction. It is more difficult to track the position of the gyre boundary in the east because of the gentler slope of the meridional temperature gradient and fewer number of sites. However, Sverdrup balance implies that the gyre boundary in the west of the basin should respond to the integrated wind stress curl across the entire basin. Therefore, the observation of a southward shift in the basin-wide gyre boundary observed in the west holds regardless of how we interpret changes in the east of the basin.

Compiling all available Mg/Ca and $U^{k'}_{37}$ SST data (supporting information) reveals a very similar pattern of temperature changes to the foraminiferal $\delta^{18}O$ data (Figure 2c). At the LGM, the SPG shows a slight warming or no change and the STG shows a slight cooling, while transition zone sites on both the east and west of the basin show an anomalously large cooling, supporting the southward extension of cold subpolar waters during glacial times.

Analysing the North Pacific %Opal compilation of Kohfeld and Chase (2011) over the last deglaciation reveals that, while the SPG and STG show a decrease in %Opal during the LGM, sites in the transition zone show a ~25% increase in %Opal on both sides of the basin (Figure 2d). This pattern is consistent with nutrient-rich subpolar waters moving further south during the LGM and increasing local productivity. The southward extension of the SPG provides a solution to the long-standing question of why, while productivity decreased throughout the SPG during

LGM, it increased in the modern day location of the transition zone between the gyres (Kienast *et al*., 2004), leading to an anti-phased pattern of productivity between the SPG and transition zone over glacial-interglacial cycles (Figure S10).

3.2 LGM General Circulation Model Simulations

Every model within the PMIP3 ensemble analysed exhibits a southward shift of the gyre boundary under glacial forcings relative to pre-industrial, with an ensemble mean change of 2.7° in the zonal-mean position of $\Psi_{barotropic} = 0$ (Figures 3 and 4), in excellent agreement with our reconstruction. Consistent with the proxy data, most models show a greater shift in the east of the basin, with a model mean southward shift of 3.4°, and a smaller change in the west of 2.3° (Fig. 4c). In the models this southward shift in the southern boundary of the SPG is caused by an overall expansion of the gyre; there is no change in the location of the northern edge of the gyre, which remains at the northern boundary of the basin. In addition to the expansion of the gyre, the models show a substantial increase in gyre strength, with an ensemble mean $\Psi_{barotropic}$ increase of 8.2 Sv (maximum north of 40°). The expansion and strengthening of the subpolar gyre circulation appear tightly coupled across all models and forcings (Figure 4). This coupling of the expansion and strengthening of the gyre arises as both processes are driven by changes in wind stress curl, rather than through a mechanistic link based on gyre dynamics.

The PMIP3 ensemble demonstrates a 2.8° southward shift in the latitude of maximum westerly wind stress in the east of the basin, but little change in the west of the basin (Figure 3); this southward shift the westerly winds is in keeping with early modelling work which demonstrated a southward displacement of the westerly jet during the LGM (e.g. Manabe & Brocolli, 1985; Bartlein et al., 1998). A southward shift in the position of the easterlies – such that they blow over the northern boundary of the North Pacific during the LGM, rather than over the Bering Straits and Sea as they do today (Gray *et al*., 2018) – drives a large increase in the zonal wind stress over the subpolar gyre (50% increase in the west of the basin and 100% increase in the east of the basin). The combined effect of the increase in easterly wind stress and the southward shift and increase in westerly wind stress is a large increase in wind stress curl across the subpolar gyre (Gray *et al*., 2018), with a southward expansion in positive wind stress curl in the east of the basin. This southward expansion in positive wind stress curl in the east drives the southward expansion of the subpolar gyre across the entire basin because the circulation is, to a good approximation, in Sverdrup balance and therefore reflects the zonal integral of $\nabla \times \tau$ from the eastern boundary of the basin (Sverdrup, 1947; Hautala *et al*., 1994; Deser *et al*., 1999; Wunsch, 2011).

To investigate which forcing(s) ultimately drive the wind stress and gyre circulation changes during the LGM, we analysed HadCM3 model runs with individual LGM forcings from greenhouse gases, ice sheet albedo, ice sheet topography, and combined ice sheet albedo and topography (Figure 4). Substantial changes in the position of $\nabla \times \tau = 0$ and $\Psi_{barotropic} = 0$ are only seen with the combined effects of ice sheet topography and albedo; ice sheet topography or ice sheet albedo alone have very little effect, as do greenhouse gases. This result illustrates a large non-linearity in the response of atmospheric circulations to ice sheet forcing; this is the result of the distinct and differing seasonality in the response of the atmosphere over the Pacific to ice sheet forcing, with albedo having the greatest effect in summer and topography having the greatest effect in winter (Roberts *et al.,* 2019).

Note that a further shift in the gyre boundary is seen with the addition of greenhouse gas forcing (Figure 4), again exceeding that expected from the sum of the individual responses and suggesting a further non-linear response to the combined ice sheet and greenhouse gas forcings (e.g. Broccoli and Manabe, 1987).

The expansion of the subpolar gyre, and associated cold waters, drives a large cooling in the mid-latitudes south of the modern-day gyre boundary. The contraction and expansion of the gyre therefore act to amplify temperature changes in the mid-latitudes over glacial-interglacial cycles. The strengthening of the SPG would increase poleward heat transport and may play a role in driving the relative warmth of the SPG during the LGM (Figure 2). A modern analogue is the Pacific Decadal Oscillation 'warm' phase, which results from a strengthening of the subpolar gyre in response to a deepening of the Aleutian Low due to stochastic fluctuations (Wills *et al.*, 2019). The gyre strengthening thus acts to dampen temperature changes in the high-latitudes over glacial-interglacial cycles.

The glacial increase in wind stress curl seen within the model ensemble would drive a large increase in Ekman suction within the subpolar gyre (Gray *et al.*, 2018). Given the close association of the wind stress curl changes driving the expansion and strengthening of the subpolar gyre, we suggest that the proxy evidence for a ~3° southward shift in the gyre boundary is also indirect evidence for a glacial increase in Ekman suction within the subpolar gyre. The impact of this increased Ekman suction on surface ocean nutrients and CO_2 over deglaciation is discussed in detail in Gray *et al.*, 2018. Increased Ekman suction would also increase the salinity of the SPG with increased upwelling of salty subsurface waters (e.g. Warren, 1983). Furthermore, both the strengthening of the gyre circulation (via increased eddy transport from the salty STG gyre and the reduced residence time of water in the SPG; Emile-Geay *et al.*, 2003) and the reorganisation of the atmosphere (lower precipitation in the SPG due to the southward shift in the jet stream and atmospheric river events e.g. Laine *et al*. 2009; Lora *et al.*, 2017) would increase the salinity of the SPG. The reorganisation of the atmosphere and gyre circulation in response to ice sheet forcing may therefore play an important role in pre-conditioning basin for the enhanced overturning circulation observed within the North Pacific during glacial periods (e.g. Keigwin, 1998; Matsumoto et al., 2002; Knudson and Ravelo, 2015; Max et al., 2017), and points towards a weakening of the North Pacific halocline, rather than a strengthening, under glacial climates (c.f. Haug *et al*., 1999).

3.3 Deglaciation

Considering all of the $\delta^{18}O$ data from east and west of 180° together, our reconstruction shows the gyre boundary begins to migrate northward beginning at ~17-16 ka, during Heinrich Stadial 1 (HS1) (Fig. 5d). The boundary then appears relatively constant during the Bølling-Allerød (14.8-12.9 ka; B/A) with a second major shift north at ~12 ka, during the latter part of the Younger Dryas. There is reasonable agreement between the timing of the gyre migration in the data and the deglacial model runs, which show the majority of the change occurring between ~16.5-12 ka (Fig. 5e); however, the model shows a steady change, rather than the two-step change in the data. We speculate this is a due to the lack of routed freshwater into the North Atlantic within these model runs, via its effects on hemispheric temperature asymmetry through heat transport. The timing also agrees with evidence of lake level changes in western North America (Fig. 5c; see below) and other

Pacific-wide changes in atmospheric circulation during the deglaciation (Russell *et al*., 2014; McGee *et al*., 2014; Jones *et al*., 2018).

However, assessing the $\delta^{18}O$ data from the east and west of the basin separately reveals a large difference in timing; the majority of the change occurs earlier in the deglaciation in the east of the basin (~16.5-14 ka) whereas the majority of the change occurs later in the deglaciation in the west of the basin (~12.5 – 10.5 ka). This east-west difference in timing can be seen in the raw $\delta^{18}O_{calcite}$ data (Figure 1) and is too large to be explained by age model uncertainty. Contrary to the data, HadCM3 shows no difference in the timing of the northward shift of the gyre boundary between the east and west, although the weakening of the westerlies does occur substantially later in the west of the basin (compared to the east) within the model (Fig. 5g).

The northward migration of the gyre boundary in the east of the basin beginning at ~16.5 ka indicates the westerly winds in the east of the basin began to shift northward at this time, concomitant with the recession of the Laurentide Ice Sheet (Lambeck *et al.*, 2014). Such a change in atmospheric circulation within the east of the basin at this time is in good agreement with records of hydroclimate in southwestern North America (Figure 5c; Bartlein *et al*., 1998; Lyle *et al*., 2012; Ibarra *et al*., 2014; McGee *et al*., 2015; Oviatt, 2015; Lora *et al*., 2016; Shuman & Serravezza, 2017; Bhattacharya *et al.*, 2018; McGee *et al.*, 2018), and suggests a clear role for dynamics in driving the observed changes in hydroclimate. However, given Sverdrup balance, changes in wind stress curl within the east of the basin should propagate across the basin and drive changes in the position of the gyre boundary in the west, and, as noted above, only a small change is seen in the west of the basin at this time.

One possible dynamical explanation for the observed difference in the timing between the east and west of the basin is that the jet stream became less zonal (i.e. more tilted) during this period, and as such, the northward shift in the westerlies in the east did not result in a substantial change to the integrated wind stress curl across the basin, resulting in a less zonal (i.e. more tilted) gyre. A more tilted jet stream does not seem unreasonable given the large changes in the size of the North American ice sheets beginning at this time (e.g. Lambeck *et al*., 2014), and is in good agreement with terrestrial proxy records and paleoclimatic simulations of this time period (Wong et al., 2016; Lora et al., 2016). Increased heat transport from a more tilted gyre could help explain the anomalous warmth of the SPG during the Bølling-Allerød (e.g. Gray *et al.*, 2018), and may help drive wider northern-hemisphere warming at this time. We note that the tilt of the gyre in the modern North Atlantic is poorly simulated by climate models (Zappa *et al*., 2013), and thus it may also be poorly simulated in the North Pacific. We also note the other models (besides HadCM3) better simulate the larger gyre boundary shift in the east relative to the west under glacial forcing (Fig. 4c), and thus may better simulate gyre tilt.

6. Conclusions

Using a basin wide compilation of planktic foraminiferal δ^{18}O data we show that the boundary between the North Pacific subpolar and subtropical gyres shifted southward by ~3° during the Last Glacial Maximum, consistent with sea surface temperature and productivity proxy data. This expansion of the North Pacific subpolar gyre is evident within all PMIP3 climate models forced with glacial boundary conditions. The models suggest that this expansion is associated with a substantial strengthening of the subpolar gyre. The strengthening of the subpolar gyre is driven by an increase in wind stress curl within the subpolar gyre resulting from a southward shift and strengthening of the mid-latitude westerlies in the east of the basin, and a southward shift in the polar easterlies across the basin. The expansion of the gyre is driven by a southward expansion of the area of positive wind stress curl within the east of the basin, due to the southward shift in the westerlies. Using model runs with individual forcings, we demonstrate that the changes in wind stress curl and associated expansion and strengthening of the subpolar gyre are a response to the combined effects of ice sheet albedo, ice sheet topography, and CO_2. Changes are small in climate model simulations where albedo and topography are forced separately, compared to their combined effects, illustrating the highly non-linear nature of the response of atmospheric circulation to ice sheet forcing (e.g. Löfverström *et al*., 2014; Roberts *et al*., 2019).

The southward expansion of the subpolar gyre would have brought nutrient-rich waters further south, explaining why productivity increased in the transition zone between the gyres while decreasing throughout the subpolar gyre during LGM. The expansion and contraction of the subpolar gyre acts as a mechanism to amplify temperature changes in the mid-latitudes over glacial-interglacial cycles. On the contrary, the strengthening of the subpolar gyre would increase poleward heat transport, warming the north of the basin and dampening temperature changes in the high-latitudes over glacial-interglacial cycles. The strengthening of the gyre circulation, in conjunction with increased Ekman suction (Gray *et al*., 2018), and reduced precipitation (Lora *et al.*, 2017), would also make the subpolar gyre saltier, weakening the halocline under glacial climates (c.f. Haug *et al.*, 1999).

Our gyre-boundary reconstruction offers a constraint on the position of the mid-latitude westerly winds over the last deglaciation and suggests the westerly winds began to shift northward at ~17-16 ka, during Heinrich Stadial 1, as the Laurentide Ice Sheet receded. This reorganisation of atmospheric circulation likely drove the large changes in hydroclimate within southwestern North America (e.g. Lora *et al.*, 2016), and may be related to other changes in atmospheric circulation seen at this time across the whole Pacific, deep into the tropics and the Southern Hemisphere (e.g. D'Agostino et al., 2017; Jones et al., 2018).

Acknowledgments

We are grateful to Lloyd Keigwin for imparting the wisdom 'If the signal is big enough, you'll see it in the 18O of calcite'. We acknowledge the World Climate Research Programme's Working Group on Coupled Modelling for the coordination of CMIP and thank the climate modelling groups for producing and making available their model output (https://esgf-node.llnl.gov/search/cmip5/). Insightful and constructive comments from two anonymous reviewers very much improved a previous version of this manuscript. WRG, JWBR and AB were funded Natural Environment Research Council (NERC) grant NE/N011716/1 awarded to JWBR and AB. RCJW was funded by the Tamaki Foundation, NASA (Grant NNX17AH56G), and NSF (Grant AGS-1929775). RFI was funded by a NERC Independent Research Fellowship NE/K008536/1. The planktic foraminiferal $\delta^{18}O$ compilation used in this study will be available on Pangea.

References

Bartlein, P.J., Anderson, K.H., Anderson, P.M., Edwards, M.E., Mock, C.J., Thompson, R.S., Webb, R.S., Webb, T., Whitlock, C, 1998. Paleoclimate simulations for North America over the past 21,000 years; features of the simulated climate and comparisons with paleoenvironmental data. Quaternary Science Reviews 17, 549-585.

Boyer, T.P., Antonov, J.I., Baranova, O.K., Coleman, C., Garcia, H.E., Grodsky, A., John- son, D.R., Locarnini, R.A., Mishonov, A.V., O'Brien, T.D., Paver, C.R., Reagan, J.R., Seidov, D., Smolyar, I.V., Zweng, M.M., 2013. World Ocean Database 2013. In: Levitus, Sydney (Ed.), Alexey Mishonov (Technical Ed.), NOAA Atlas NESDIS, vol. 72. 209 pp.

Braconnot, P., Harrison, S.P., Kageyama, M., Bartlein, P.J., Masson-Delmotte, V., Abe-Ouchi, A., Otto-Bliesner, B. and Zhao, Y., 2012. Evaluation of climate models using palaeoclimatic data. Nature Climate Change, **2**(6), 417-424.

Broccoli, A.J., Manabe, S., 1987. The influence of continental ice, atmospheric CO2, and land albedo on the climate of the last glacial maximum. Climate Dynamics **1**, 87-99.

D'Agostino, R., P. Lionello, O. Adam,and T. Schneider (2017), Factors controlling Hadley circulation changes from the Last Glacial Maximum to the end of the 21st century. Geophysical Research Letters **44**, 8585-8591. doi:10.1002/2017GL074533.

Deser, C., Alexanders, M. A., Timlin, M. S., 1999. Evidence for a Wind-Driven Intensification of the Kuroshio Current Extension from the 1970s to the 1980s. Journal of Climate **12**, 1697-1706.

Emile-Geay, J., Cane, M.A., Naik, N., Seager, R., Clement, A.C., van Geen, A. (2003) Warren revisited: Atmospheric freshwater fluxes and 'Why is no deep water formed in the North Pacific'. Journal of Geophysical Research **108**, doi:10.1029/2001JC001058.

Forget, G, Ferreira, D, 2019. Global ocean heat transport dominated by heat export from the tropical Pacific. *Nature Geoscience*, https://doi.org/10.1038/s41561-019-0333-7,

Gray, W.R., Rae, J.W.B, Wills, R.C.J., Shevenell, A.E., Taylor, B., Burke, A., Foster, G.L., Lear, C.H., 2018. Deglacial upwelling, productivity and CO2 outgassing in the North Pacific Ocean. Nature Geoscience **11**, 340–344.

Haug, G.H., Sigman, D.M., Tiedemann, R., Pedersen, T.F., Sarnthein M., 1999. Onset of permanent stratification in the subarctic Pacific Ocean. Nature 40, 779-782.

Huatala, S.L., Roemmich, D.H., Schmitz, W.J., 1994. Is the North Pacific in Sverdrup balance along 24°N? Journal of Geophysical Research 99, 16041-16052.

Ibarra, D. E., A. E. Egger, K. L. Weaver, C. R. Harris, and K. Maher, 2014: Rise and fall of late Pleistocene pluvial lakes in response to reduced evaporation and precipitation: Evidence from Lake Surprise, California. Geol. Soc. Amer. Bull., 126, 1387–1415, https://doi.org/10.1130/B31014.1.

Ivanovic, R.F., Gregoire, L.J., Kageyama, M., Roche, D.M., Valdes, P.J., Burke, A., Drummond, R., Peltier, W.R., Tarasov, L., 2016. Transient climate simulations of the deglaciation 21–9 thousand years before present (version 1) PMIP4 Core experiment design and boundary conditions. Geosci. Model Dev. **9**, 25632587. https://doi.org/10.5194/gmd-9-2563-2016.

Jones, T.R., Roberts, W.H.G., Steig, E.J., Cuffey, K.M., Markle, B.R., White, J.W.C (2018) Southern Hemisphere climate variability forced by Northern Hemisphere ice-sheet topography. Nature **554**, 351-355.

Keigwin, L., 1998. Glacial-age hydrography of the far northwest Pacific Ocean. Paleoceanography **13**, 323–339.

Key, R.M., Olsen, A., van Heuven, S., Lauvset, S.K., Velo, A., Lin, X., Schirnick, C., Kozyr, A., Tanhua, T., Hoppema, M., Jutterström, S., Steinfeldt, R., Jeansson, E., Ishi, M., Perez, F.F., Suzuki, T., 2015. Global Ocean Data Analysis Project, Version 2 (GLODAPv2). ORNL/CDIAC-162, ND-P093. Carbon Dioxide Information Analysis Center, Oak Ridge National Laboratory, US Department of Energy, Oak Ridge, Tennessee. https://doi.org/10.3334/CDIAC/OTG.NDP093_GLODAPv2. http://cdiac.ornl.gov/oceans/GLODAPv2/NDP_093.pdf.

Kim, S. and O'Neil, J. (1997). Equilibrium and nonequilibrium oxygen isotope effects in synthetic carbonates. Geochimica et Cosmochimica Acta **61**, 3461–3475.

Kirby, M. E., S. J. Feakins, N. Bonuso, J. M. Fantozzi, and C. A. Hiner, 2013. Latest Pleistocene to Holocene hydroclimates from Lake Elsinore, California, Quat. Sci. Rev., 76, 1–15.

Knudson, K. P. and Ravelo, A. C., 2015. North Pacific Intermediate Water circulation enhanced by the closure of the Bering Strait. Paleoceanography **30**, PA002840.

Kohfeld, K. E. & Chase, Z., 2011. Controls on deglacial changes in biogenic fluxes in the North Pacific Ocean. Quat. Sci. Rev. **30**, 3350–3363.

Lambeck, K., Rouby, H., Purcell, A., Sun, Y., Sambridge, M., 2014. Sea level and global ice volumes from the Last Glacial Maximum to the Holocene. Proc. Natl Acad. Sci. USA **111**, 15296–15303.

LeGrande, A.N., Schmidt, G.A., 2006. Global gridded data set of the oxygen isotopic composition in seawater. Geophys. Res. Lett. **33**, L12604.

Li, C., Battisti, D.S., 2008. Reduced Atlantic Storminess during Last Glacial Maximum: Evidence from a Coupled Climate Model. Journal of Climate **21** 3561-3579. DOI: 10.1175/2007JCLI2166.1.

Lora, J. M., J. L. Mitchell, Tripati, A. E., 2016. Abrupt reorganization of North Pacific and western North American climate during the last deglaciation, Geophys. Res. Lett., 43, 11,796–11,804, doi:10.1002/2016GL071244.

Lora, J. M., 2018. Components and Mechanisms of Hydrologic Cycle Changes over North America at the Last Glacial Maximum. Journal of Climate 31, 7035-7051.

Löfverström, M., R. Caballero, J. Nilsson, Kleman, J., 2014. Evolution of the large-scale atmospheric circulation in response to changing ice sheets over the last glacial cycle. Climate of the Past **10**, 1453-1471.

Lyle, M., Heusser, L., Ravelo, C., Yamamoto, M., Barron, J., Diffenbaugh, N. S., Herbert, T., Andreasen, D., 2012. Out of the Tropics: The Pacific, Great Basin Lakes, and Late Pleistocene Water Cycle in the Western United States. Science, **337**, 1629-1633.

Lynch-Stieglitz, J., Curry, W.B., Slowey, N. (1999) Weaker Gulf Stream in the Florida Straits during the Last Glacial Maximum. Nature **402**, 644-648.

Manabe, S., Broccoli, A.J., 1985. The influence of Continental Ice Sheets on the Climate of an Ice Age. Journal of Geophysical Research 90, 2167-2190.

Marcott, S.A. *et al*., 2014. Centennial-scale changes in the global carbon cycle during the last deglaciation. Nature **514**, 617-619. doi:10.1038/nature13799

Matsumoto, K., Oba, T. & Lynch-Stieglitz, J., 2002. Interior hydrography and circulation of the glacial Pacific Ocean. Quat. Sci. Rev. **21**,1693–1704.

Max, L., Rippert, N., Lembke-Jene, L., Mackensen, A., Nürnberg, D., Tiedemann, R., 2017. Evidence for enhanced convection of North Pacific Intermediate Water to the low-latitude Pacific under glacial conditions. Paleoceanography **32**, 41–55.

McGee, D., Quade, J., Edwards, R.L, Broecker, W.S., Cheng, H., Reiners, P.W., Evenson, N., 2012. Lacustrine cave carbonates: Novel archives of paleohydrologic change in the Bonneville Basin (Utah, USA). Earth and Planetary Science Letters **351-352**, 182-194.

McGee, D., Donohoe, A., Marshall, J., Ferreira, D. (2014) Changes in ITCZ location and cross-equatorial heat transport at the Last Glacial Maximum, Heinrich Stadial 1, and the mid-Holocene. Earth and Planetary Science Letters **390**, 69-79.

McGee, D., Moreno-Chamarro, E., Marshall, J., Galbraith, E.D. (2018) Western U.S. lake expansions during Heinrich stadials linked to Pacific Hadley circulation. Science Advances 4, eaav0118.

Morris, P.J., Swindles, G.T., Valdes, P.J., Ivanovic, R.F., Gregoire, L.J., Smith, M.W., Tarasov, L., Haywood, A.M., Bacon, K.L., 2018. Global peatland initiation driven by regionally asynchronous warming. PNAS 201717838. https://doi.org/10.1073/pnas.1717838115.

Nelson, S.T., Wood, M.J., Mayo, A.L., Tingey, D.G., Eggett, D., 2005. Shoreline tufa and tufaglomerate from Pleistocene Lake Bonneville, Utah, USA: stable isotopic and mineralogical records of lake conditions, processes, and climate. Journal of Quaternary Science **20**, 3–19.

Okazaki, Y., Timmermann, A., Menviel, L., Harada, N., Abe-Ouchi, A., Chikamoto, M., Mouchet, A., and Asahi, H., 2010. Deepwater Formation in the North Pacific During the Last Glacial Termination. Science **329**, 200-204.

Oster, J.L., Ibarra, D.E., Winnick, M.J., Maher, K., 2015. Steering of westerly storms over western North America at the Last Glacial Maximum. Nature Geoscience **8**, 201-205.

Oviatt, C. G., R. S. Thompson, D. S. Kaufman, J. Bright, and R. M. Forester, 1999. Reinterpretation of the Burmester Core, Bonneville Basin, Utah, Quat. Res., 52, 180–184.

Oviatt, C. G., 2015. Chronology of Lake Bonneville, 30,000 to 10,000 yr B.P. Quaternary Science Reviews 110, 166-171.

Pausata, F. S. R., Li, C., Wettstein, J. J., Kageyama, M., and Nisancioglu, K. H., 2011. The key role of topography in altering North Atlantic atmospheric circulation during the last glacial period, Clim. Past **7**, 1089-1101, https://doi.org/10.5194/cp-7-1089-2011.

Rae, J. W. B., Sarnthein, M., Foster, G. L., Ridgwell, A., Grootes, P. M., and Elliott, T., 2014. Deep water formation in the North Pacific and deglacial CO2 rise. Paleoceanography **29**, 645–667.

Roberts, W. H. G., Valdes, P. J., 2017. Green Mountains and White Plains: The Effect of Northern Hemisphere Ice Sheets on the Global Energy Budget. Journal of Climate **30**, 3887- 3905. DOI: 10.1175/JCLI-D-15-0846.1.

Roberts, W.H.G., Li, C., Valdes, P.J., 2019. The mechanisms that determine the response of the Northern Hemisphere's stationary waves to North American ice sheets. Journal of Climate, https://doi.org/10.1175/JCLI-D-18-0586.1

Russell, J.M., Russell, Vogel, H., Konecky, B.L., Bijaksana, S., Huang, Y., Melles, M., Wattrus, N., Costa, K., King, J.W., 2014. Glacial forcing of central Indonesian hydroclimate since 60,000 yr BP. Proc. Natl Acad. Sci. USA 111, 5100–5105.

Sawada, K. and Handa, N., 1998. Variability of the path of the Kuroshio ocean current over the past 25,000 years. Nature **392**, 592–595.

Schrag, D. P., Adkins, J. F., McIntyre, K., Alexander, J. L., Hodell, D. A., Charles, C. D. McManus, J. F., 2002. The oxygen isotopic composition of seawater during the Last Glacial Maximum. Quaternary Science Reviews **21**, 331-342.

Shuman, B.N., Serravezza, M., 2017. Patterns of hydroclimatic change in the Rocky Mountains and surrounding regions since the last glacial maximum. Quaternary Science Reviews 173, 58-77.

Sverdrup, 1947. Wind-Driven Currents in a Baroclinic Ocean; with Application to the Equatorial Currents of the Eastern Pacific. PNAS **33**, 318–26.

Taylor, K. E., R. J. Stouffer, and G. A. Meehl, 2012: An overview of CMIP5 and the experiment design. Bull. Am. Meteorol. Soc., **93** (4), 485–498

Thompson and Shackleton, 1980. North Pacific palaeoceanography: late Quaternary coiling variations of planktonic foraminifer Neogloboquadrina pachyderma. Nature **287**, 829–833.

Warren, B.A. (1983) Why is no deep water formed in the North Pacific? Journal of Marine Research **41**, 327-347.

Wills, R. C. J., Battisti, D. S., Proistosescu, C., Thompson, L., Hartmann, D. L., & Armour, K. (2019). Ocean circulation signatures of North Pacific decadal variability. Geophysical Research Letters, 46. https://doi.org/10.1029/2018GL080716

Wong, C. I., G. L. Potter, I. P. Montañez, B. L. Otto-Bliesner, P. Behling, and J. L. Oster (2016), Evolution of moisture transport to the western U.S. during the last deglaciation, Geophys. Res. Lett., 43, 3468–3477, doi:10.1002/2016GL068389.

Wood, S.N. (2011) Fast stable restricted maximum likelihood and marginal likelihood estimation of semiparametric generalized linear models. Journal of the Royal Statistical Society (B) **73**, 3-36.

Wood, S.N., Pya N., Säfken, B. (2016) Smoothing Parameter and Model Selection for General Smooth Models, Journal of the American Statistical Association, 111:516, 1548-1563, DOI: 10.1080/01621459.2016.1180986

Wunsch, C., 2011. The decadal mean ocean circulation and Sverdrup balance. Journal of Marine Research 69, 417-434.

Zappa, G., L.C. Shaffrey, and K.I. Hodges (2013) The Ability of CMIP5 Models to Simulate North Atlantic Extratropical Cyclones. Journal of Climate **26**, 5379–5396, https://doi.org/10.1175/JCLI-D-12-00501.1

Figure 1 Planktic foraminiferal $\delta^{18}O$ versus age with core site latitude represented by colour. Data are divided east **(b)** and west **(a)** of 180°. HS1, B/A and YD are Heinrich Stadial 1 (14.8-17.5 ka), Bølling-Allerød (12.9-14.8 ka) and the Younger Dryas (11.8-12.9 ka), respectively. **(c)** gridded $\delta^{18}O_{water}$ from LeGrande and Schmidt (2006) **(d)** calcite-water fractionation calculated using WOA13 mean annual temperature (Boyer et al., 2013) and the temperature-fractionation relationship of Kim and O'Neil (1997) **(e)** predicted $\delta^{18}O_{calcite}$ using (c) and (d) (note the colour scale is the same for all three panels) **(f)** slope of the zonal-mean meridional gradient in $\delta^{18}O_{water}$, $\delta^{18}O_{calcite\text{-}water}$ and $\delta^{18}O_{calcite}$ The steepest part of the meridional $\delta^{18}O_{calcite}$ gradient is lies at the gyre boundary, and is a result of the large temperature difference between the gyres.

Figure 2 (a) Holocene (open symbols, dashed line) and LGM (filled symbols, solid line) foraminiferal $\delta^{18}O$ data versus latitude – symbols reflect species of planktic foraminifera (see panel b). Foraminiferal $\delta^{18}O$ values have been corrected for whole ocean changes in $\delta^{18}O_{water}$ due to changes in terrestrial ice volume and the mean ocean change in SST from the PMIP3 ensemble ($\delta^{18}O_{ivc}$; see Methods). The data are fit with a general additive model (see Methods), with the standard error (68% and 95%) of the fit shown **(b)** as in (a), however with data separated east and west of 180° **(c)** Compiled LGM-Holocene SST differences versus latitude, based on Mg/Ca and $U^{k'}_{37}$: Open symbols/dashed line is LGM proxy SST minus modern climatological SST. Filled symbols/solid line is LGM proxy SST minus Holocene proxy SST **(d)** Compiled %Opal from Kohfeld and Chase (2011) data, shown as a ratio of LGM/Holocene versus latitude, with a value of greater than 1 indicating a glacial increase. In (c) and (d) the data are fit with a general additive model, with the standard error of fit (68%) shown.

Figure 3 PMIP3 ensemble mean of **(a)** LGM-PI zonal windstress (τu), with the PI climatology indicated by contours (contour interval of 0.04 N m^2; dashed is negative and solid is positive), **(b)** zonal average and averages east and west of 180° of zonal windstress in LGM and PI, **(c)** LGM-PI barotropic streamfunction ($\Psi_{barotropic}$), with the PI climatology indicated by contours (contour interval of 10 Sv; dashed is negative and solid is positive), **(d)** zonal average and averages east and west of

180° of the barotropic streamfunction in LGM and PI **(e)** LGM-PI SST anomaly from global mean, with the PI climatology indicated by the contours **(f)** zonal average and averages east and west of 180° of the SST anomaly from global mean in the LGM and PI.

Figure 4 (a) LGM-PI change in latitude of zonal-mean $\Psi_{barotropic} = 0$ versus change in longitudinally weighted mean $\nabla \times \tau$ (τ_{curl}) across the southern boundary of the subpolar gyre (38-50 °N) **(b)** LGM-PI change in latitude of zonal mean $\Psi_{barotropic} = 0$ versus change in $\Psi_{barotropic}$ within the subpolar gyre (maximum north of 40°) **(c)** LGM-PI change in latitude of zonal mean $\Psi_{barotropic} = 0$ east and west of 180°. Green Mountains = LGM ice sheet topography with PI albedo, White Mountains = LGM ice sheet albedo with PI topography, White Mountains = LGM ice sheet topography and albedo.

Figure 5 (a) Sealevel curve of Lambeck *et al.* (2014) and sealevel equivalent of global and North American ice sheet volume in the ICE6Gc ice sheet reconstruction **(b)** Atmospheric $p\mathrm{CO}_2$ record of Marcott *et al*. (2014) and $p\mathrm{CO}_2$ forcing used in model **(c)** north-westward progression of lake high stands in southwestern North America (McGee *et al*., 2018) **(d)** reconstructed change in gyre boundary position with 1σ uncertainty (east and west is east and west of 180°) **(e)** modelled change in gyre boundary position **(f)** modelled change in subpolar gyre strength (maximum north of 40°) **(g)** modelled change in westerly position (determined as latitude of maximum zonal windstress, τu) **(h)** modelled change in westerly strength (determined as maximum τu) **(i)** modelled change in wind stress strength exerted by the easterlies (determined as mean τu between 50-60 °N). For model results solid lines denote a change in position, and the dashed lines denote a change in strength. See Figure S8 for meridional profiles of (g), (h), and (i).

Figure 1.

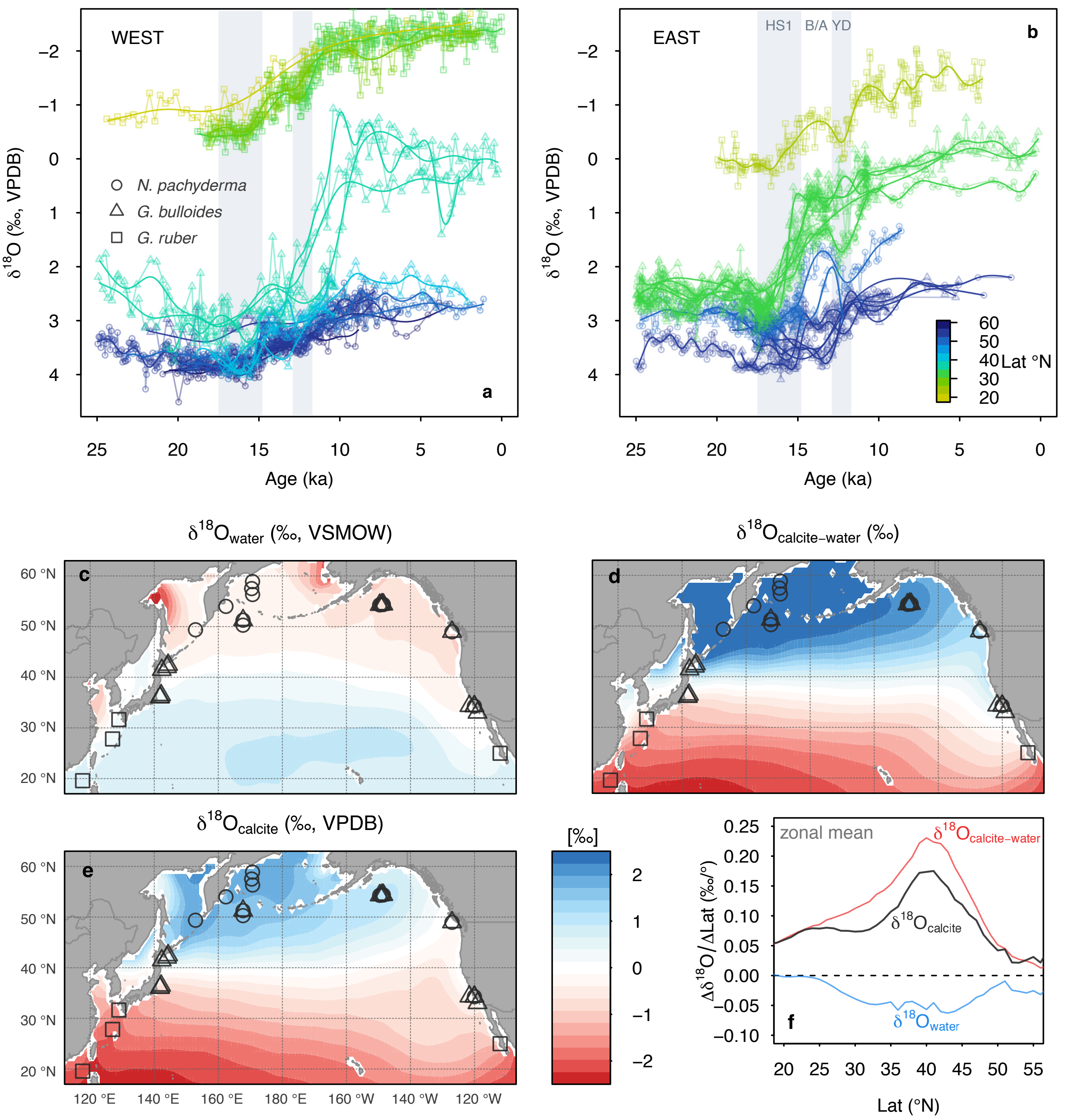

WEST
a
N. pachyderma
G. bulloides
G. ruber
δ18O (‰, VPDB)
Age (ka)
EAST
HS1
B/A
YD
b
Lat °N
δ18Owater (‰, VSMOW)
c
δ18Ocalcite−water (‰)
d
δ18Ocalcite (‰, VPDB)
e
[‰]
zonal mean
δ18Ocalcite−water
δ18Ocalcite
δ18Owater
f
Δδ18O/ΔLat (‰/°)
Lat (°N)

Figure 2.

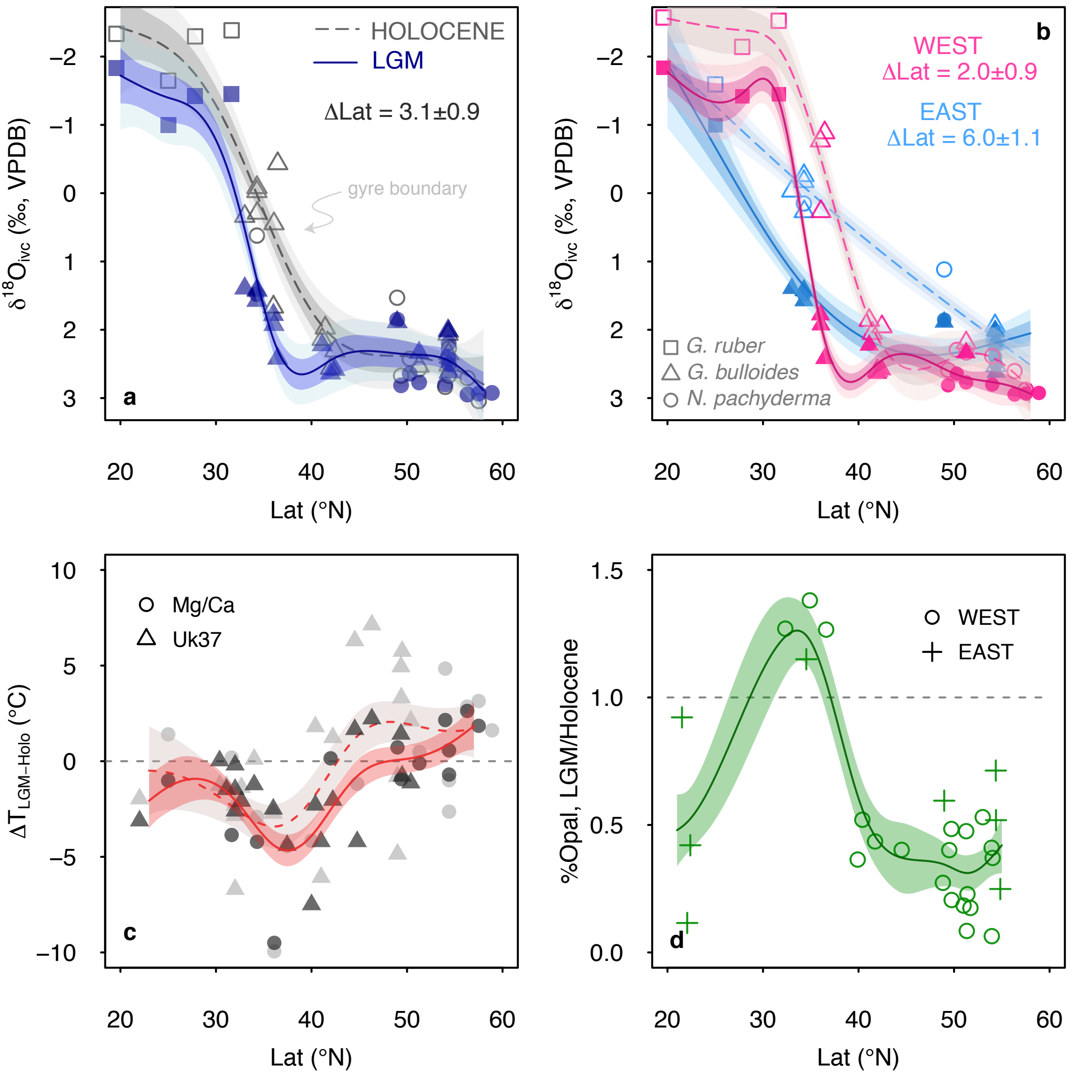

HOLOCENE
LGM
ΔLat = 3.1±0.9
gyre boundary
a
δ18Oivc (‰, VPDB)
Lat (°N)
b
WEST
ΔLat = 2.0±0.9
EAST
ΔLat = 6.0±1.1
G. ruber
G. bulloides
N. pachyderma
δ18Oivc (‰, VPDB)
Lat (°N)
Mg/Ca
Uk37
c
ΔTLGM−Holo (°C)
Lat (°N)
WEST
EAST
d
%Opal, LGM/Holocene
Lat (°N)

Figure 3.

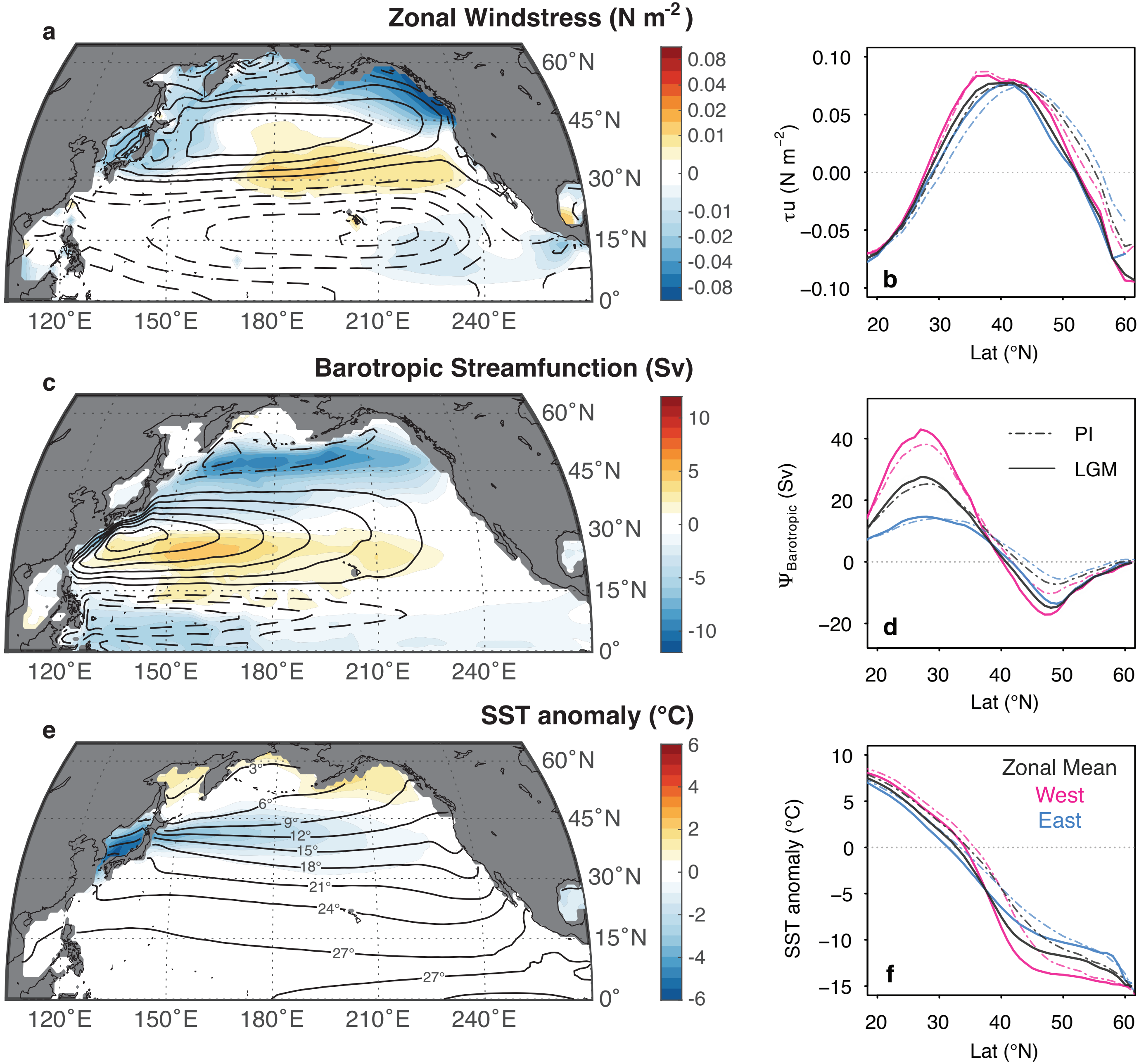

Zonal Windstress (N m^{-2})
a
b
τu (N m^{-2})
Lat (°N)
Barotropic Streamfunction (Sv)
c
d
$\Psi_{Barotropic}$ (Sv)
PI
LGM
SST anomaly (°C)
e
f
SST anomaly (°C)
Zonal Mean
West
East
120°E
150°E
180°E
210°E
240°E
0°
15°N
30°N
45°N
60°N

Figure 4.

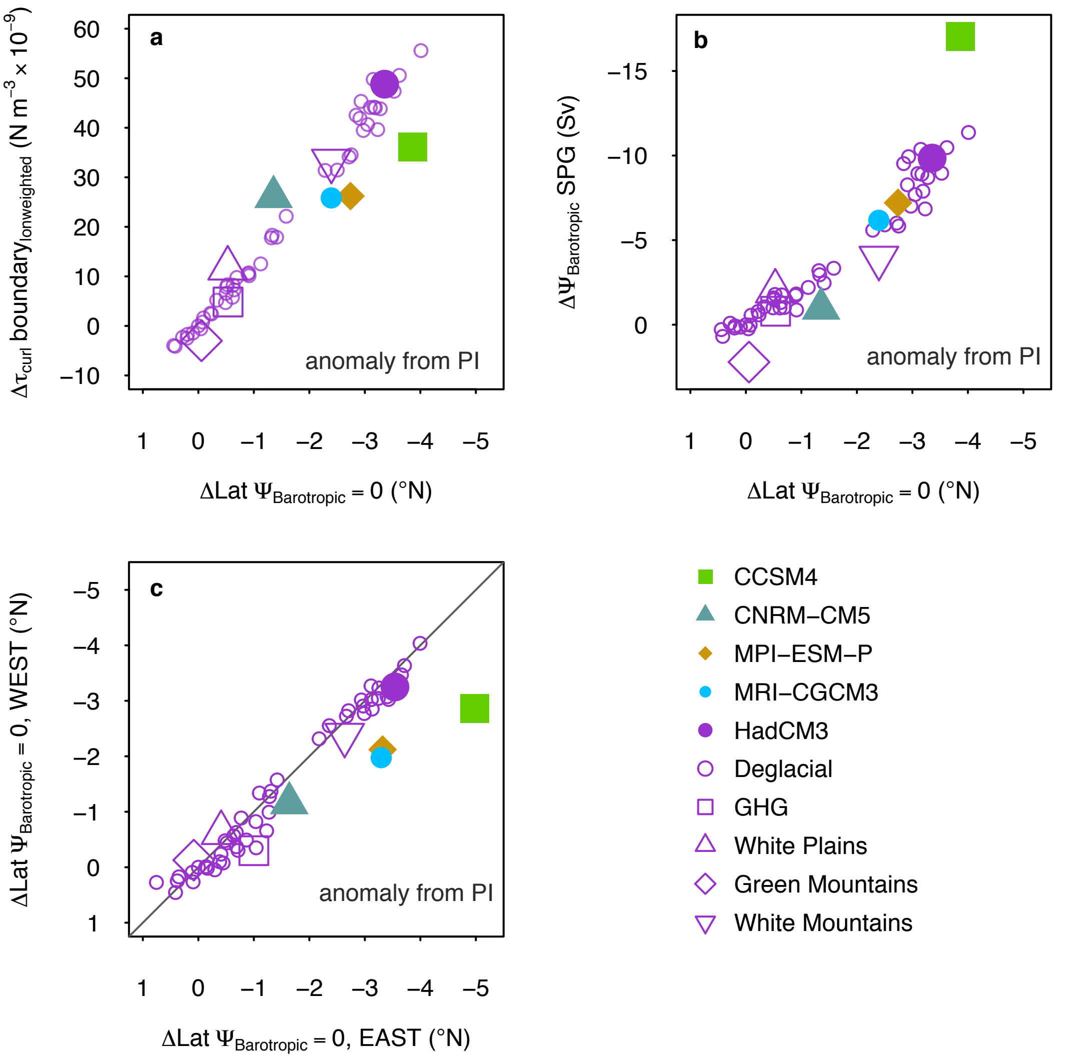
a
b
c
anomaly from PI
anomaly from PI
anomaly from PI
$\Delta\tau_{curl}$ boundary$_{lonweighted}$ (N m^{-3} × 10^{-9})
$\Delta\Psi_{Barotropic}$ SPG (Sv)
ΔLat $\Psi_{Barotropic}$ = 0 (°N)
ΔLat $\Psi_{Barotropic}$ = 0 (°N)
ΔLat $\Psi_{Barotropic}$ = 0, WEST (°N)
ΔLat $\Psi_{Barotropic}$ = 0, EAST (°N)
CCSM4
CNRM−CM5
MPI−ESM−P
MRI−CGCM3
HadCM3
Deglacial
GHG
White Plains
Green Mountains
White Mountains

Figure 5.

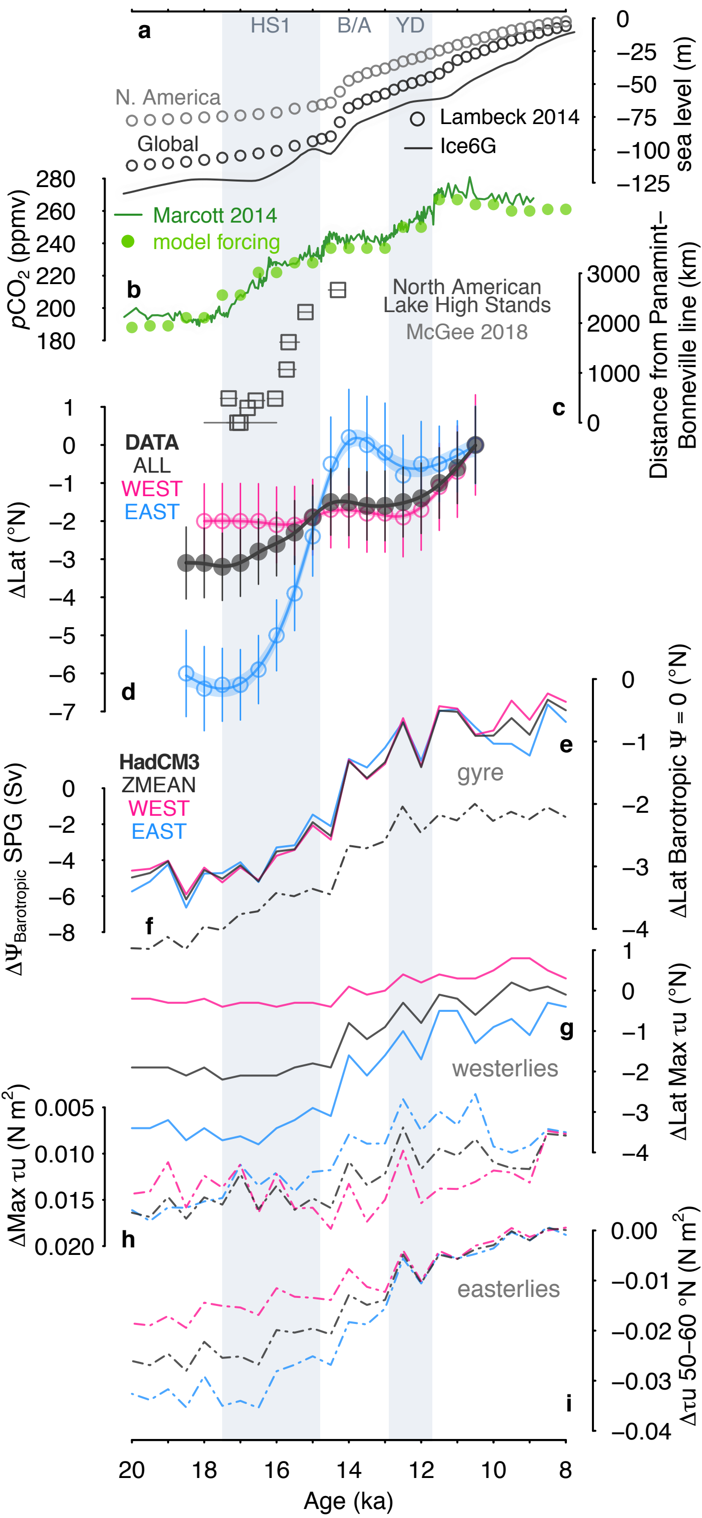

HS1
B/A
YD
a
N. America
Global
Lambeck 2014
Ice6G
sea level (m)
b
Marcott 2014
model forcing
pCO$_2$ (ppmv)
North American Lake High Stands
McGee 2018
c
Distance from Panamint–Bonneville line (km)
d
DATA
ALL
WEST
EAST
ΔLat (°N)
e
gyre
ΔLat Barotropic Ψ = 0 (°N)
f
HadCM3
ZMEAN
WEST
EAST
$\Delta\Psi_{Barotropic}$ SPG (Sv)
g
westerlies
ΔLat Max τu (°N)
h
ΔMax τu (N m^2)
i
easterlies
Δτu 50–60 °N (N m^2)
Age (ka)